



HAL
open science

Full-scale optic designed for onsite study of damage growth at the Laser MegaJoule facility

Chloé Lacombe, Laurent Lamaignère, Guillaume Hallo, Martin Sozet, Thierry Donval, Gérard Razé, Christel Ameil, Mélusine Benoit, Florian Gaudfrin, Edouard Bordenave, et al.

► To cite this version:

Chloé Lacombe, Laurent Lamaignère, Guillaume Hallo, Martin Sozet, Thierry Donval, et al.. Full-scale optic designed for onsite study of damage growth at the Laser MegaJoule facility. *Optics Express*, 2023, 31 (3), pp.4291-4305. 10.1364/OE.474581 . hal-04308275

HAL Id: hal-04308275




<https://cnrs.hal.science/hal-04308275v1>

Submitted on 27 Nov 2023

HAL is a multi-disciplinary open access archive for the deposit and dissemination of scientific research documents, whether they are published or not. The documents may come from teaching and research institutions in France or abroad, or from public or private research centers.

L'archive ouverte pluridisciplinaire **HAL**, est destinée au dépôt et à la diffusion de documents scientifiques de niveau recherche, publiés ou non, émanant des établissements d'enseignement et de recherche français ou étrangers, des laboratoires publics ou privés.

Full-scale optic designed for onsite study of damage growth at the Laser MegaJoule facility

CHLOÉ LACOMBE,^{1,*}  LAURENT LAMAIGNÈRE,¹ GUILLAUME HALLO,^{1,2}  MARTIN SOZET,¹ THIERRY DONVAL,¹ GÉRARD RAZÉ,¹ CHRISTEL AMEIL,¹ MÉLUSINE BENOIT,¹ FLORIAN GAUDFRIN,¹ EDOUARD BORDENAVE,¹ NICOLAS BONOD,³ AND JÉRÔME NÉAUPORT¹ 

¹CEA CESTA, 15 avenue des Sablières, CS 60001, F-33116, Le Barp, France

²Université Paris-Saclay, ENS Paris-Saclay, CNRS, LMT - Laboratoire de Mécanique et Technologie, 91190 Gif-sur-Yvette, France

³Aix Marseille Univ, CNRS, Centrale Marseille, Institut Fresnel, Marseille, France

*Chloe.Lacombe@cea.fr

Abstract: Large fusion scale laser facilities aim at delivering megajoules laser energy in the UV spectrum and nanosecond regime. Due to the extreme laser energies, the laser damage of final optics of such beamlines is an important issue that must be addressed. Once a damage site initiates, it grows at each laser shot which decreases the quality of the optical component and spoils laser performances. Operation at full energy and power of such laser facilities requires a perfect control of damage kinetics and laser parameters. Monitoring damage kinetics involves onsite observation, understanding of damage growth process and prediction of growth features. Facilities are equipped with cameras dedicated to the monitoring of damage site growth. Here we propose to design and manufacture a dedicated full size optical component to study damage growth at increased energy, on the beamline, *i.e.* in the real environment of the optics on a large laser facility. Used for the first time in 2021, the growth statistics acquired by this approach at the Laser MegaJoule (LMJ) facility provides a new calibration point at a fluence less than 5 J cm^{-2} and a flat-in-time pulse of 3 ns.

© 2023 Optica Publishing Group under the terms of the [Optica Open Access Publishing Agreement](#)

1. Introduction

High power laser facilities such as the National Ignition Facility (NIF), the ShenGuang-III (SG-III) and the Laser MegaJoule (LMJ) are designed to achieve fusion by inertial confinement [1–3]. For each laser beam, multi-kilojoule ultraviolet laser energy with a pulse duration in the nanosecond range is required. Laser Megajoule will be equipped with 176 laser beams to perform high energy density physics experiments, including fusion experiments up to 1.4 MJ at 351 nm in a few nanoseconds. All the beams are carried and focused at the center of a 10 m diameter target chamber. The first 11 bundles of 8 beams are currently in operation for experiments at an energy level of $\sim 3.75 \text{ kJ per laser beam}$. This low energy operation is needed to limit maintenance while new laser beamlines are still mounted and commissioned for a full LMJ completion.

Final optical components are exposed to multi-kJ ultraviolet (351 nm) laser energy with nanosecond pulse duration and a laser beam size of about 1000 cm^2 . These fused silica optics may damage under such extreme laser conditions. Laser damage is defined as a permanent change of the optical component induced by the laser beam. In LMJ laser conditions, the laser damage morphology is a crater of diameter of about $10 \mu\text{m}–30 \mu\text{m}$ with sub-surface fractures [4–7]. Laser damage initiation is due to a combination of loading induced by the UV laser beam [8] and random defects [9,10] or self-focusing [11] or even particulate contamination [12,13] on the optics surface. On LMJ, final optics are of three types: ultraviolet focusing gratings, focusing

and separating the main wavelength useful for the experiment from the residual wavelengths of the frequency conversion system; vacuum windows, isolating the vacuum of the experiment chamber from the rest of the facility, and debris-shield optics, protecting other optics from target debris. Once a damage site has initiated on an optic, it may grow at each new laser shot when the laser energy is greater than the growth threshold [5], which is usually the case for fusion scale laser facilities. Damage growth is defined as the increase of damage area and depth for successive laser shots. Damaged optics directly affect the laser performance required to perform the experiments [5,14] and generate damage on downstream optics since damage sites can result in a local overintensification of the laser beam [15,16]. To maintain a specific laser quality and to preserve other optics, optical components with too degraded performances must be replaced.

To extend the operation lifetime of these optics, two methods have been developed to stop the damage growth. (i) The so-called local laser blocker that consists in locally reducing the beam fluence under the growth threshold [17,18]. In order not to impact the total beam energy for the experiments, this technique is limited to about ten beam blockers per optic at the location of the damage sites. (ii) The Carbon Dioxide (CO₂) laser optics mitigation that consists in machining a cone with a CO₂ laser to remove the damage site fractures and thus to stop the damage growth [19–21]. This operation cannot be performed directly on the facility and requires maintenance of the optical component. As CO₂ laser optics mitigation is possible as long as the damage equivalent diameter remains under 750 μm, the laser blockers process must be optimized by detecting the most critical damage sites by combining their diameter and their growth dynamics.

To track damage sites of final optics, laser damage is managed with images acquired by a high resolution camera (4096 × 4096 pixels) set in the center of the vacuum chamber after each laser shot [18]. The imaging system is similar to those in NIF [22] and SG-III [23] facilities. A schematic view of this onsite observation system is shown in Fig. 1. These optics, *i.e.* gratings and vacuum windows, are illuminated by two LEDs mounted on one edge of the optics, red LEDs for gratings and green ones for vacuum windows. Laser damage sites scatter the light emitted by the LEDs, and a part of this scattered light is collected by an objective lens that images gratings or vacuum windows on a CCD sensor at a distance of 8 m. The image sensor converts the collected light energy into grayscale images. Images (one example is shown in Fig. 2) acquired by this system consist of a black background with bright spots corresponding to damage sites. The dynamics of the grey levels is between 0 and 2¹⁶ (14 bits).

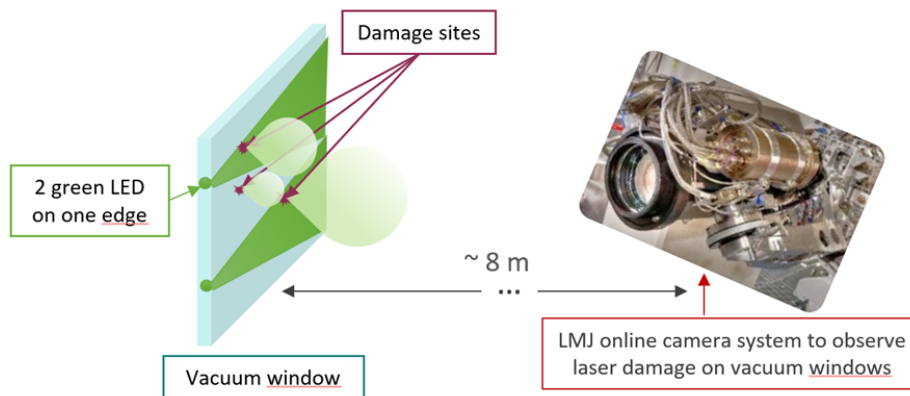


Fig. 1. Schematic view of LMJ onsite image acquisition system for vacuum window.

The spatial resolution, *i.e.*, the size of one pixel of the image projected in the object plane, is $\sim 100 \mu\text{m}$. The bare measurement of the site diameter does not reach the accuracy level required to characterize the growth of damage sites before they reach the mitigation equivalent diameter limit

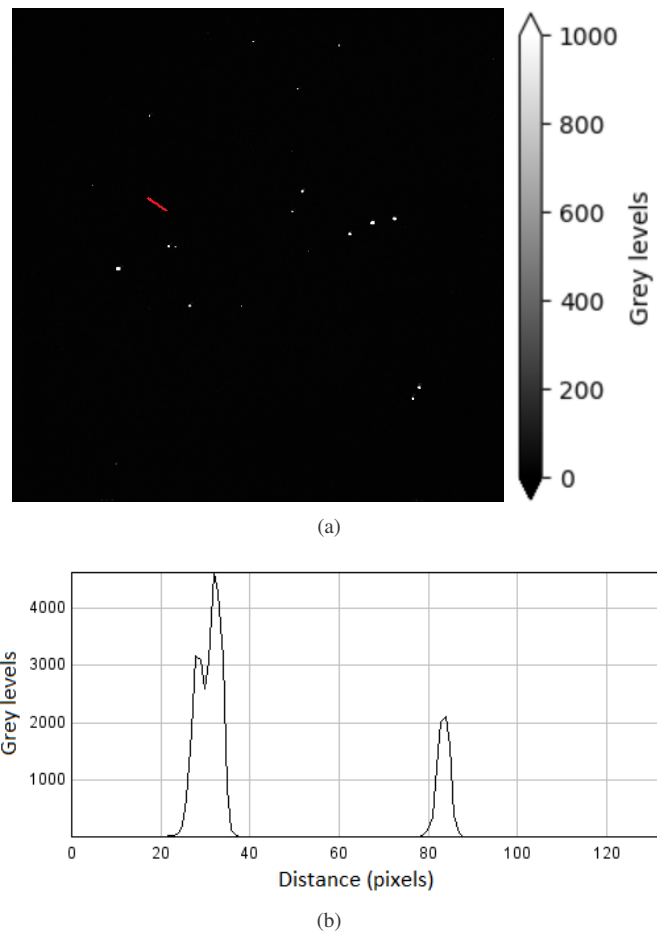


Fig. 2. (a) Example of LMJ vacuum window image with large damage sites. The gray levels of the image correspond to the amount of light collected by the sensor of the camera. To better distinguish damage sites, the display dynamics range between 0 and 1000 but all gray levels are used to process these images. The red line, that crosses two damage sites, symbolizes the section extracted from the displayed image and shown in (b).

(750 μm). Previous works have shown that the grey levels of acquired images are directly related to the damage equivalent diameter [22,24]. This technique provides a much higher accuracy on the estimated damage equivalent diameter than counting the number of lit pixels.

The control of the damage process is crucial for facility operation at full energy [15]. The stability and homogeneity of the laser beam itself are key parameters and require a strict limitation of both spatial and temporal overintensifications [25]. The knowledge of the physical models that describe initiation and growth of damage sites is also a key factor to anticipate the needs of maintenance and to optimize the operational use of the facility [5,15,26]. The literature on damage laws is based on data acquired with laboratory experiments [4,5,26–31]. Models used to predict the damage growth onsite are based on a large amount of feedback statistics directly acquired on the facility [32]. For a better knowledge of damage phenomenon on the facility, we aim at establishing the laser damage laws directly on a LMJ beamline with a dedicated component. The current study focus on studying damage growth at LMJ enhanced energy from 3.75 kJ to 4.7 kJ with dedicated LMJ experimental campaigns. Let us notice that the very high quality of LMJ optic surfaces strongly limit the probability of damage sites. In order to fully get profit of these performance campaigns with a limited number of laser shots and laser beams, a specific component was defined and used. A matrix of nearly 1000 damage sites was initiated on a vacuum window on a offline laser damage set-up. This component was precisely measured on a metrology bench before being mounted on the LMJ facility for the duration of the campaign. It was precisely measured in laboratory again after its removal from the facility. This component composed of a matrix of damage sites was very useful for the calibration of the LMJ onsite monitoring camera to accurately link the grey levels of light scattering by damage sites and their size (equivalent circle diameter) as detailed by Hallo [24]. The number of new damage sites and the quantification of the growth statistics of the damage sites composing the matrix provide useful calibration points for damage models at an energy level higher than that of the current operation. The great advantage of this experiment is its representativeness to a component mounted on a real laser beam and exposed to mechanical and environmental constraints.

The paper is organized as follows. The design, manufacturing process and characterization of the matrix of damage sites and the characteristics of the laser shots are first presented in Section 2. The combination of the large number of damage sites on the matrix with the properties of the laser beam provides a damage growth probability and a growth rate distribution that are detailed and discussed in Section 3.

2. Matrix of damage sites

On LMJ facility, UV laser beam enters in the experiment chamber through a vacuum window that ensures the vacuum containment in the experimental chamber. The ease of maintenance and observation of its state of damage is the reason of the choice of this component for the realization of the damage matrix. A vacuum window is a square fused silica sol gel coated optic polished using high damage resistance finishing process [14,33,34] of ~ 40 cm side and 3.4 cm thickness.

The main goal of the damage monitoring is to accurately quantify the growth dynamics of damage sites before they reach the mitigation equivalent diameter limit (*i.e.*, 750 μm). Damage sites diameter are expected between 30 μm and 300 μm to cover the whole range of dimensions to be studied, taking into account their growth during the campaign. The number of damage sites in the matrix is conditioned by the need to keep them independent despite their growth, as well as the respect of the safety criterion which limits the total damaged area. The chosen distance between two damage sites is 1.2 cm. As reported in some studies about the morphologies and dimensions of the damage sites in volume [27,35], the fractures do not extend beyond the apparent diameter of the damage site that is observed on the surface. Thus, the growth information alone is sufficient to determine the damage sites spacing. In addition to damage sites, the matrix includes mitigation cones for onsite validation of the mitigation process.

The matrix is made of 31×31 elements including 31 mitigation cones for a total of 930 damage sites. The distribution of the damage sites dimensions, shown in Fig. 3, was also chosen to calibrate the detection capabilities of the LMJ onsite camera at any point of the component (see Ref. [24] for more details). Damage sites actually initiated have equivalent diameters between $10 \mu\text{m}$ and $500 \mu\text{m}$.

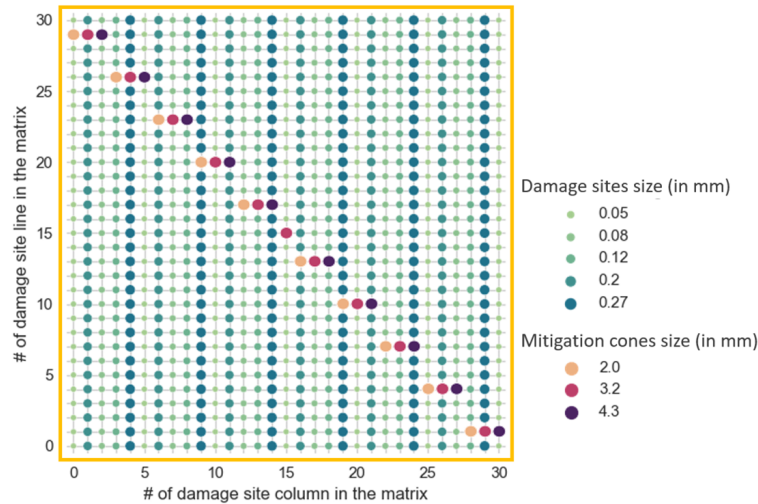


Fig. 3. Distribution of the damage sites on the matrix according to their equivalent diameter range in green to blue scale and mitigation cone in color scale. Spatial scale is not representative of the distance between damage sites which is 1.2 cm . The yellow frame materializes the edges of the optics. Damage sites cover the whole optics, up to the edge of the component.

2.1. Damage site initiation

Laser damage sites are realized off-line on a laser damage bench called ELAN [36]. This set-up is designed to reproduce the configuration yielding onsite damage initiations: The laser system is selected for its characteristics close to those of the LMJ (*i.e.*, wavelength of 355 nm and pulse length of 7.5 ns) and the beam is collimated over the entire thickness of the optical component. Thus the shape and the diameter of the laser beam are the same on the front and on the rear surfaces of the component. In this configuration, the damage site is initiated on the rear face with the same dynamics and the same phenomenology as in onsite conditions. The beam is spatially Gaussian with a diameter of the order of $700 \mu\text{m}$ at $1/e$. For thick optical components, the main challenges to initiate rear surface damage are to avoid Kerr and Brillouin nonlinear processes. Non-linear Kerr propagation could lead to the formation of not requested bulk damage such as filaments. Brillouin non-linear propagation could lead to the initiation of front surface damage due to back stimulated Brillouin scattering, also not desired in this study [30]. These difficulties are resolved by controlling the intensity profiles of the laser pulses. A phase-modulated injection seeder allows operating the nanosecond Nd:YAG Q-switched laser with pulses having both a large spectral bandwidth and a smooth temporal waveform. Because of the smooth temporal waveform, such pulses reduce the impact of the Kerr effect and, because of the large spectral bandwidth, suppress stimulated Brillouin scattering [37]. Once these non-linear processes are mastered, damage sites are initiated at fluences ensuring a probability of damage close to 100% , *i.e.*, fluences of the order of 30 J cm^{-2} at 7.5 ns corresponding to fluences close to 20 J cm^{-2} at 3 ns considering the temporal scale law in $\tau^{0.5}$ for damage initiation [38]. With these fluences,

the diameters of damage sites range between $\sim 30\ \mu\text{m}$ and $\sim 100\ \mu\text{m}$. Such fluences are also chosen in order to trigger unique damage sites (*i.e.*, only one damage site is created at each shot), corresponding more or less to the top of the spatially Gaussian beam where the energy density is the strongest. The damage sites thus created are not representative of all the damage sites that can occur at a facility like the LMJ. They are, however, representative of the most critical damage sites, those that will grow and it is this population of damage sites that is studied.

To obtain larger damage sites, between $100\ \mu\text{m}$ and $300\ \mu\text{m}$, damage sites are irradiated with few additional shots to grow the damage up to the selected equivalent diameter. The fluences of the shots and the number of shots are chosen based on the previously measured growth coefficients [27]. Initiation, growth and equivalent diameter of the damage sites are monitored in real time after each shot thanks to a visualization through a macroscope. The entire procedure is first tested and validated on a dedicated optical component. Next, following this protocol, a 31×31 damage matrix is made on the vacuum window. The damage sites thus obtained have diameters ranging between $\sim 10\ \mu\text{m}$ and $\sim 500\ \mu\text{m}$. Growing the damage sites at a lower fluence also has the advantage of providing laser damage sites more representative of that naturally generated on the LMJ.

2.2. Off-line metrology of damage sites

Before its installation on LMJ facility and after its removal, the matrix of damage sites is observed on dedicated optical set-up [39]. The component is illuminated from the edge and the light scattered by damage sites is collected by the observation system on the same basic principle as the onsite system. Two types of highly spatially resolved systems are available. The first one cover the whole component by sub-images to reconstitute a complete image with a resolution of $\sim 10\ \mu\text{m}$. The second one is a long front macroscope, motorized (zoom and focus) and coupled to a coaxial illumination, with a resolution of $\sim 2\ \mu\text{m}$ by pixel [39]. This resolution allows for an accurate characterization of defects or damage sites. It is used only for a selection of ~ 70 damage sites. These precise measurements are very helpful for calibrating the intensity measurements acquired at the facility and for gaining accurate knowledge of the damage site dimensions used for this study. Two damage sites seen under the macroscope before and after the LMJ onsite experiments are shown in Fig. 4.

2.3. Lifespan of the matrix of damage sites on the LMJ facility

Mounted on a laser beamline of the LMJ facility, the vacuum window with the matrix of damage sites was used during an experimental laser campaign at the end of 2021. This campaign consisted of 7 shots with an energy of $\sim 4.7\ \text{kJ}$, a flat-in-time pulse shape of 3 ns and a spatial contrast of about 8 – 10% at 1ω . The spatial contrast, defined by (1), is the ratio of the standard deviation in fluence to the mean. It is calculated on the spatial measurement of the laser beam, at the output of the amplifier section.

$$C = \frac{\sigma}{\mu}, \quad (1)$$

where C denotes the spatial contrast, σ is the standard deviation calculated from the fluence points in the measured laser beam and μ is the mean of the fluence points in the measured laser beam.

After each shot, images of investigated component were acquired by the LMJ onsite camera. The first image acquisition is shown in Fig. 5. The largest and brightest elements of the matrix that are easily visible on the diagonal of the optic are the mitigation cones.

The spatial energy distribution at 1053 nm of the LMJ laser beam was measured at the output of the amplifier section with a spatial resolution of $\sim 440\ \mu\text{m}$ for each laser shot using the onsite output sensor near-field camera. The propagation of the laser beam measured from the output of the amplifier section to the output of the vacuum window was simulated with the Miro

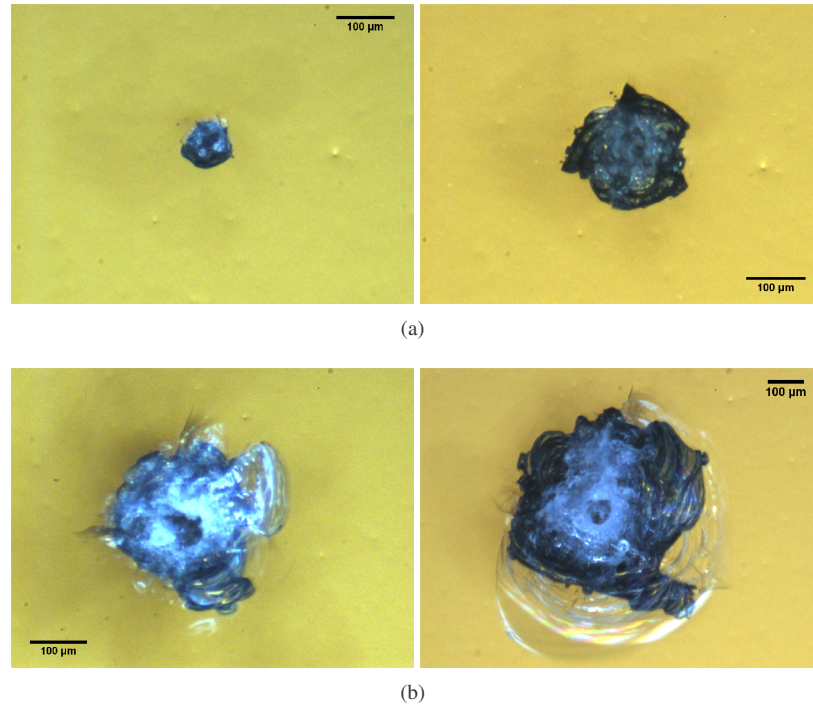


Fig. 4. Two damage sites (a) and (b) of the matrix of damage sites seen under the microscope at the beginning at left and at the end of the LMJ onsite experiments at right. On each image, the black segment has a size of 100 μm

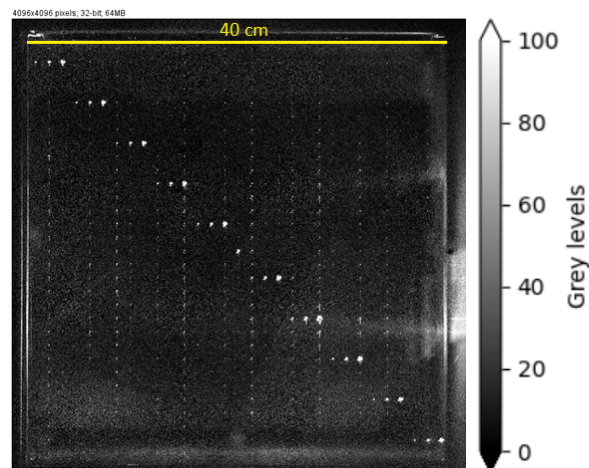


Fig. 5. Onsite image of the matrix of damage sites just after its installation on a LMJ beamline. To better distinguish the damage sites of the matrix, the display dynamics range between 0 and 100 but all grey levels from 0 to 2^{16} are used to process images.

software [40]. The calculation takes into account the optical aberrations of each individual optical component constituting the beamline [3] (transport mirrors, alignment reference optic, gratings, conversion crystals) measured by interferometry and the effects of the frequency conversion system. The result is shown in Fig. 6.

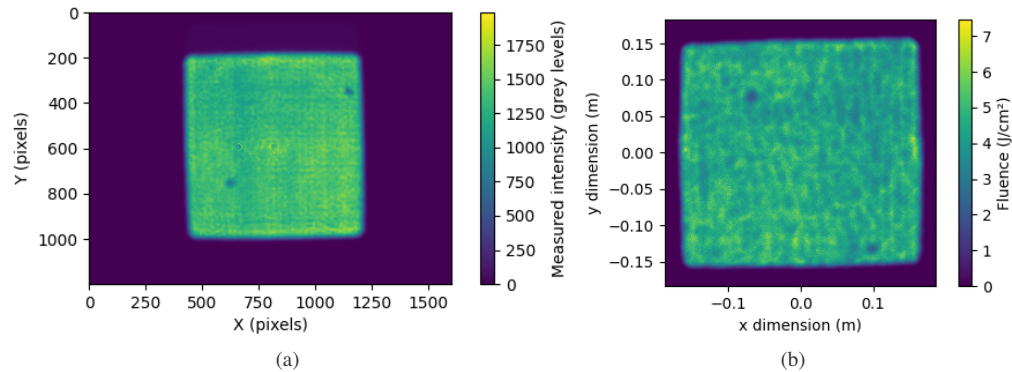


Fig. 6. Spatial distribution of the LMJ laser beam at the output of the amplifier section at 1053 nm (a) and simulated at the output of the vacuum window at 351 nm after transport section, conversion crystals and focusing grating (b) for the first shot through the matrix of damage sites.

The distribution of the fluence on the matrix of damage sites is registered to evaluate the fluence corresponding to each damage site. The registration is made from a low fluence ($\sim 1 \text{ J cm}^{-2}$) near field laser shot. The spatial transformation (translation, rotation and zoom) is computed between the image at the output of the amplifier section (Fig. 7(a)) and the image acquired by the vacuum windows damage measurement diagnostic (Fig. 7(b)) at very low energy using a grid specifically realized by the spatial shaping of the LMJ laser beam. The grid is a keyed matrix of 22 beam blockers to determine affine transforms between the two planes.

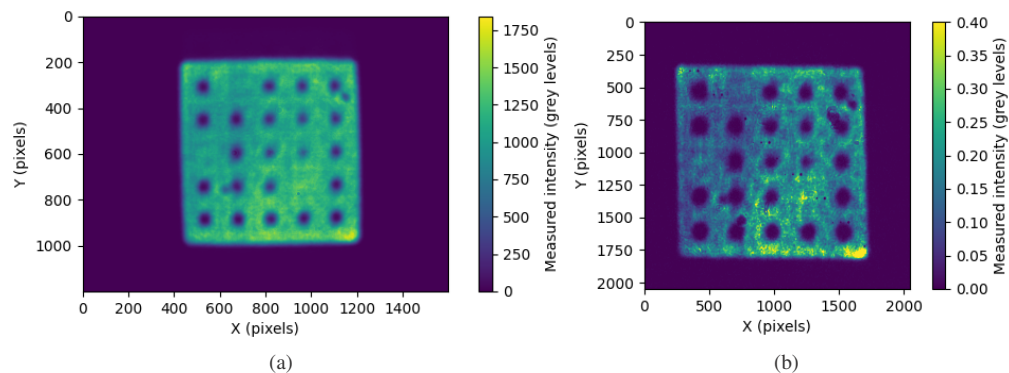


Fig. 7. The spatial transforms between images acquired at the output of the amplifier section (a) and at the level of the vacuum window (b) is computed using a grid in the laser beam spatial shape.

This spatial transformation is then used to match the simulated fluence computed with Miro to the corresponding damage sites. The fluence evaluated for each damage site is the mean fluence over 1 mm^2 , centered on the damage site.

On the vacuum windows, at 351 nm, the spatial contrast is $\sim 14\%$ and the beam area is $\sim 1000\text{ cm}^2$. The mean fluence is $\sim 4.7\text{ J cm}^{-2}$. The spatial shape of the laser beam is very stable for all 7 shots and a mean fluence is calculated for each damage site of the matrix.

3. Results

3.1. Data processing

Images can be impacted by spatial shifts, background light intensity or lighting system variations. These variations can be corrected by recent techniques based on Digital Image Correlation (DIC) principles [41]. After corrections, the pixel intensity variations from one image to another is only affected by the damage growth and the acquisition noise.

Damage sites are then detected thanks to an optimized local signal-to-noise ratio algorithm, called LASNR [42]. This algorithm permits to get rid of the background elements illuminated by the LEDs and to detect small bright elements in a noisy background. The delineation is performed for each damage site using a region-growing method also detailed in Ref. [42].

The analysis of the intensity emitted by the laser damage site that is captured by the camera brings a sub-pixel precision on the damage site dimension [22,41]. The measured intensity of a damage site is the integral of the gray levels on the delimited support. Thanks to the matrix of damage sites, the calibration of onsite acquisitions was performed by comparing, respectively, the first and the last onsite images to the highly resolved offline measurements done before the mounting of the matrix of damage sites and after its removal. These results were the reported in Ref. [24]. Intensity of a damage site is related to its dimension, *i.e.*, its effective circular diameter, by (2):

$$D = D_0 \sqrt{\frac{I}{\kappa}}, \quad (2)$$

where D denotes the diameter of the damage site, I the integrated intensity on its onsite acquisition, D_0 the physical size of one pixel ($100\text{ }\mu\text{m}$), and κ a scale parameter (equal to 3.5×10^3 gray levels for the LMJ image acquisition system).

Such image processing steps provide the dimension of each laser damage site of the matrix with a sub-pixel accuracy for all acquisitions of the laser campaign.

3.2. Visualization of the growth of damage sites

For each damage site in the matrix, the difference in dimension is calculated between the acquisition performed after each laser shot and the acquisition performed before the first laser shot. The matrices of these diameter differences are presented in Fig. 8 with the aim of visualizing the spatial distribution of growth on the matrix of damage sites over the shots.

The shot-by-shot spatial distribution images of damage sites growth shows the square area of the laser beam passage in the center of the matrix. They also show that a large amount of damage sites traversed by the beam has grown.

3.3. Growth rate calculation

For each damage site, a growth rate is calculated considering all the measurement points acquired before and after each shot. The fluences considered in this experiment being relatively low, the growth of the damage sites remains low and thus makes it possible to assimilate a unique growth rate evaluated on the whole of the 7 shots of the experiment. The evolution curve is optimized by the laser damage growth Eq. (3). Since some damage sites do not grow on the first shot, the first

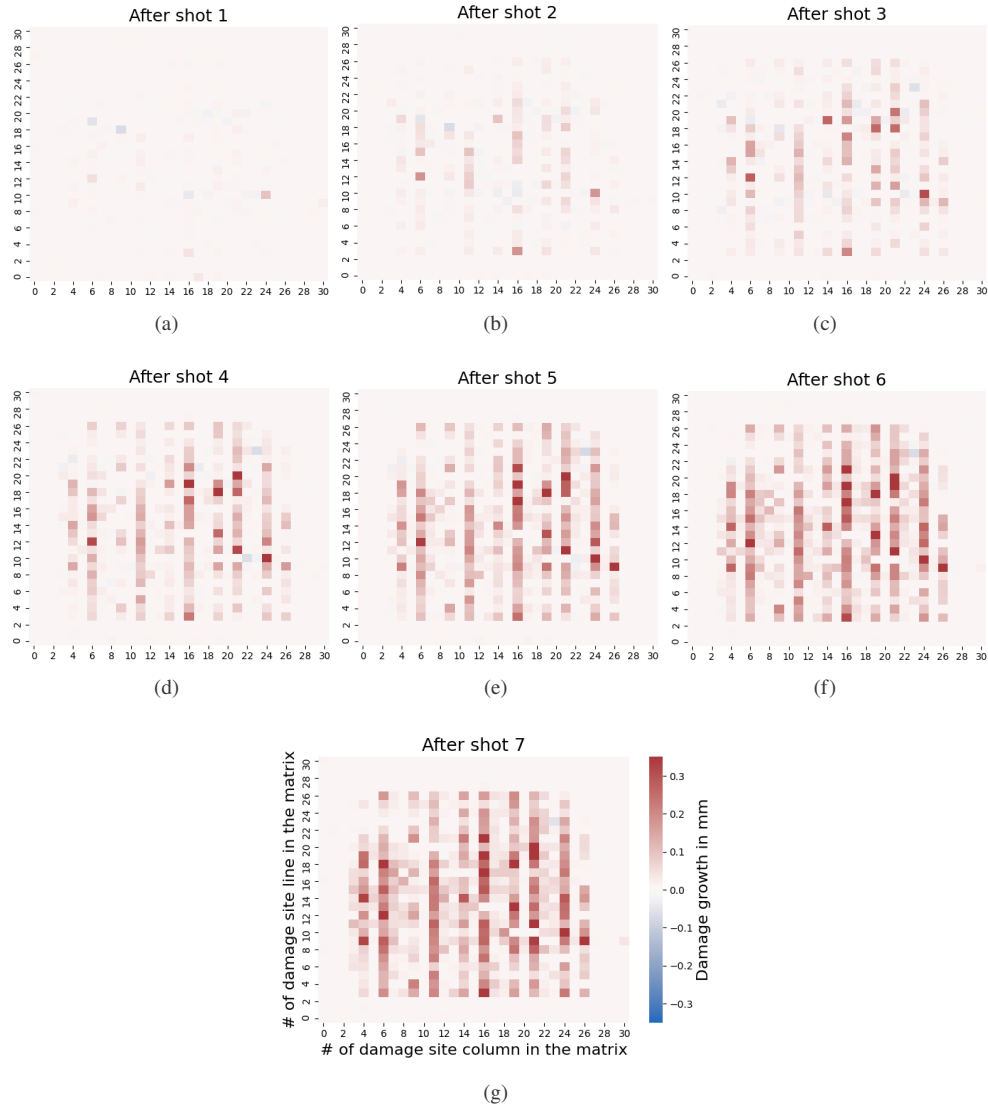


Fig. 8. Difference in diameter (in mm) for the matrix of damage sites between images acquired after each laser shot and the image acquired before the first laser shot. The axes and the color bar, only displayed on the image after the seventh shot, are identical for all figures. The negative values (in blue) are due to the precision of the evaluation of the equivalent diameter of the damage sites from the intensity measured by the camera. Damage sites on lines / columns 0 to 2 and 27 to 30 have not been exposed to the laser beam. It was therefore expected that it would not grow.

growth shot (N_{start}) has been added in the equation:

$$D = \begin{cases} D_0 \exp(\alpha (N - N_{start})) & \text{if } N \geq N_{start} \\ D_0 & \text{if } N < N_{start} \end{cases}, \quad (3)$$

where D are the measured damage site diameters after each shot, D_0 denotes the initial damage site diameter, N the shot numbers and N_{start} the number of the first shot at which the damage growth, and α is the growth rate.

For a better illustration, the growth dynamics of two damage sites are illustrated in Fig. 9 with one damage site with a growth from the third shot (a) and the second with a growth from the first shot (b).

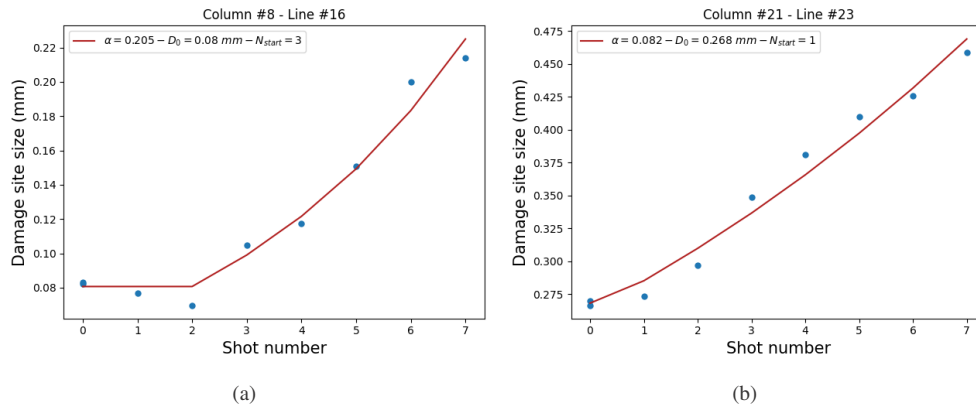


Fig. 9. Growth of damage sites with onsite measured points in blue and curve fitting represented by the red line for the two damage sites presented in Fig. 4.

For further analysis, the damage sites are classified into 4 ranges of dimensions. The number of samples per range is between 78 and 176.

3.4. Growth probability

The growth probability is evaluated for each of these ranges and is shown in Fig. 10. Only damage sites that have been exposed by a fluence higher than 4 J cm^{-2} are considered. Indeed, some damage sites in the matrix are at the edge of the laser beam, the fluence is thus intermediate and uncertain, and others are outside the laser beam. These damage sites are not part of the studied domain (at a mean fluence about 4.6 J/cm^2). They were used for verification of the measurement accuracy but are not taken into account in order not to distort the growth statistics. Mean values (blue points on the graph) are calculated by considering as growing site any damage site whose calculated growth rate is strictly positive (negative values may occur due to measurement accuracy). To evaluate the uncertainties, the accuracy of the damage growth assessment from the 8 onsite acquisitions as well as the number of representative samples are taken into account. For some damage sites, the acquisition noise may be sufficient for the growth rate to be non-zero, a minimum growth probability is then calculated by considering as non-increasing any damage whose calculated growth rate is less than 0.02, represented by orange triangles. Confidence intervals at 95%, represented by blue lines, are evaluated using the classic Eq. (4):

$$\text{error} = \sqrt{\frac{p(1-p)}{n}}, \quad (4)$$

where p is the probability of growth and n denotes the total number of damage sites in each range.

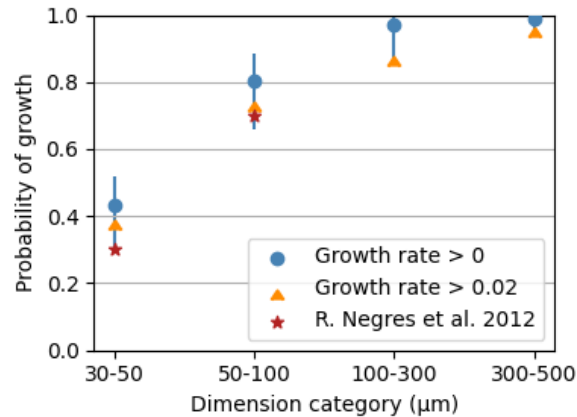


Fig. 10. Growth probability for 4 ranges of damage site equivalent diameters at 351 nm for a mean fluence of $\sim 4.7 \text{ J cm}^{-2}$ and a pulse duration of 3 ns in blue considering as growing all damage sites with a non zero growth rate and in orange all damage sites with a growth greater than 0.02. The points that are obtained in Negres *et al.* work in Ref. [28] for experiments with 5 ns pulse duration are superimposed (red stars).

The growth probabilities for a fluence of 4.7 J cm^{-2} are close to the results reported by Negres *et al.* in Ref. [28] for damage sites diameters between 30 μm and 100 μm . These experiments were performed in vacuum with a flat-in-time pulse of 5 ns. On the contrary, the growth probabilities are higher than the studies performed by Veinhard *et al.* [27] conducted in air. As suggested in Ref. [43], vacuum may have an impact on the resistance of fractures.

3.5. Growth rates distribution

The growth dynamics are evaluated for each damage site on the matrix. The distribution of the calculated growth rates is shown for each of the 4 damage equivalent diameter classes in Fig. 11.

These scatterplots show a dispersion of growth rates that decreases when the damage site equivalent diameters increase. This change in the dispersion of growth rates as a function of the size of damage sites is not captured in the Weibull distributions described in the literature, especially in Ref. [26]. Taking into account that this change in the dispersion of the growth rates could come from the accuracy of the onsite measurement, the growth rates are compared and validated with the accurate off-line measurements made before and after the experimental campaign (see Section 2). Since the rates are evaluated by considering all 8 measurements, the accuracy on the value of the growth rate does not explain the observed dispersion.

The mean value of the growth rate is evaluated for two data sets: only for strictly growing damage sites, represented by stars, and for all damage sites, represented by diamonds. Considering only growing damage sites, the mean value of the growth rate decreases as the damage sites become larger. This result is quite consistent with the observations made by Lamagnère *et al.* [4]. Considering all damage sites, mean values of the growth rates are more similar with a value of about 0.07. Equation (5) given in Ref. [5] yields the dependence of the mean value of the growth rate on the duration of the temporal shape for flat-in-time laser pulses:

$$\alpha = 0.025 \tau^{0.27} (F - 3.22 - 0.3 \tau), \quad (5)$$

where α is the mean value of the growth rates, τ denotes the duration of the laser pulse and F is the fluence. For a fluence of $\sim 5 \text{ J cm}^{-2}$, the mean value of the growth rates obtained with this equation is of ~ 0.03 for 3 ns and ~ 0.01 for 5 ns. Values obtained in different works are summarized in Table 1.

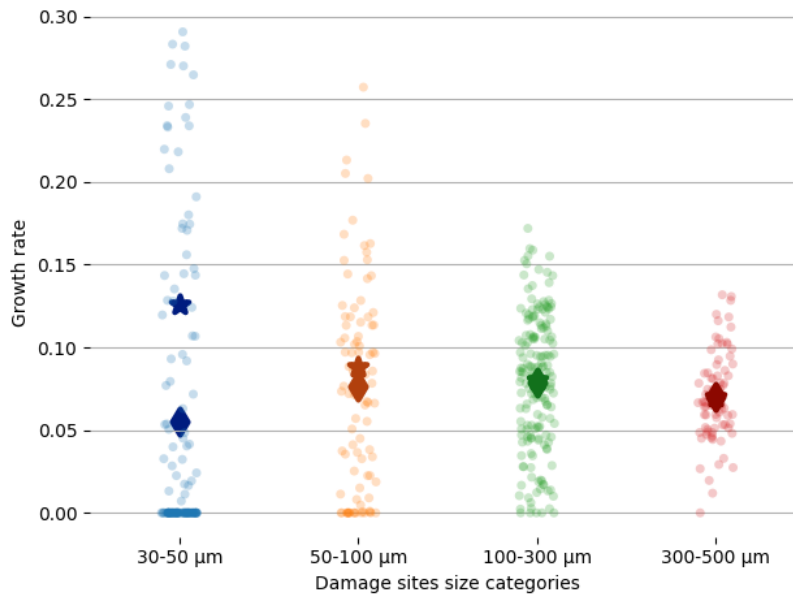


Fig. 11. Growth rate distribution for 4 ranges of damage site equivalent diameters for a mean fluence of $\sim 4.7 \text{ J cm}^{-2}$ and a pulse duration of 3 ns. Symbols. Diamonds: mean values of the growth rates considering all data including non growing damage sites; Stars: mean values of the growth rates considering growing damage sites only (*i.e.*, with a strictly positive growth rate).

Table 1. Summary of the mean growth rates for different references and the results obtained with the matrix of damage sites on LMJ at $\sim 4.7 \text{ J cm}^{-2}$.

	3 ns	5 ns
Eq. (5) Manes [5]	0.03	0.01
Negres [26] in vacuum	-	0.025-0.05
Veinhard [27] in air	0.07	-
LMJ matrix optic air/vacuum	0.06-0.08	-

Data comparison shows that the values obtained from Eq. (5) are much lower than the data acquired in Refs. [26,27] as well as for the LMJ matrix of damage sites. At 3 ns, the mean growth rate of the onsite matrix of damage sites is similar to that obtained in the experiments realized in lab in Ref. [27]. So the acquired set of data does not show any particular impact of the vacuum or air environment on the growth rate mean value. This observation should be consolidated with future data acquired on the facility for higher fluences.

Results obtained with the matrix of damage sites show that the Weibull laws defined at 5 ns should be reassessed at 3 ns. Indeed, Eq. (5) does not seem appropriate to make the conversion between 5 ns and 3 ns given the differences obtained. The set of data acquired with the matrix of damage sites for a single fluence point at $\sim 4.7 \text{ J cm}^{-2}$ is not sufficient to establish a new Weibull law. Future experiments involving this matrix of damage sites should provide data for higher fluences, which is necessary for this re-evaluation.

4. Conclusion

The LMJ optics composed of a matrix of damage sites brings a lot of results. Scattered light intensities on onsite acquisitions have been related in a simple way with the equivalent circle

diameters of the damage sites [24]. Fully representative of the LMJ environment, the growth law, both by the growth probability and by the growth rate distribution, completes the data acquired in laboratory. The data acquired with the matrix of damage sites are therefore very useful for the development of a representative phenomenological model of the LMJ vacuum windows damage growth. The size of the LMJ beam allows to have from few shots an important growth statistic, difficult to have with laboratory experiments. Future experiments planned with this matrix of damage sites should provide data for higher fluences, missing points necessary for a re-evaluation of the damage laws as close as possible to the experimental conditions in the facility. In addition, this technique could also be used for other optical components such as debris-shield optics positioned after vacuum windows for example.

Disclosures. The authors declare no conflicts of interest.

Data availability. Data underlying the results presented in this paper are not publicly available at this time but may be obtained from the authors upon reasonable request.

References

1. G. H. Miller, "The national ignition facility," in *SPIE Proceedings*, M. A. Lane and C. R. Wuest, eds. (SPIE, 2004).
2. W. Zheng, "The updated advancements of inertial confinement fusion program in china," in *CLEO: 2013*, (OSA, 2013).
3. J. Ebrardt and J. M. Chaput, "LMJ project status," *J. Phys.: Conf. Ser.* **112**(3), 032005 (2008).
4. L. Lemaître, G. Dupuy, A. Bourgeade, A. Benoist, A. Roques, and R. Courchinoux, "Damage growth in fused silica optics at 351 nm: refined modeling of large-beam experiments," *Appl. Phys. B* **114**(4), 517–526 (2014).
5. K. R. Manes, M. L. Spaeth, and J. J. Adams, *et al.*, "Damage mechanisms avoided or managed for NIF large optics," *Fusion Sci. Technol.* **69**(1), 146–249 (2016).
6. D. Ristau, "Laser-induced damage in optical materials," Boca Raton - London - New York (2015).
7. S. G. Demos, M. Staggs, and M. R. Kozlowski, "Investigation of processes leading to damage growth in optical materials for large-aperture lasers," *Appl. Opt.* **41**(18), 3628–3633 (2002).
8. M. Veinhard, O. Bonville, S. Bouillet, E. Bordenave, R. Courchinoux, R. Parreault, J.-Y. Natoli, and L. Lemaître, "Effect of non-linear amplification of phase and amplitude modulations on laser-induced damage of thick fused silica optics with large beams at 351 nm," *J. Appl. Phys.* **124**(16), 163106 (2018).
9. N. Bloembergen, "Role of cracks, pores, and absorbing inclusions on laser induced damage threshold at surfaces of transparent dielectrics," *Appl. Opt.* **12**(4), 661–664 (1973).
10. J. Neauport, P. Cormont, P. Legros, C. Ambard, and J. Destribats, "Imaging subsurface damage of grinded fused silica optics by confocal fluorescence microscopy," *Opt. Express* **17**(5), 3543–3554 (2009).
11. M. J. Soileau, W. E. Williams, N. Mansour, and E. W. V. Stryland, "Laser-Induced Damage And The Role Of Self-Focusing," *Opt. Eng.* **28**(10), 1133–1144 (1989).
12. D. M. Kane and D. R. Halfpenny, "Reduced threshold ultraviolet laser ablation of glass substrates with surface particle coverage: A mechanism for systematic surface laser damage," *J. Appl. Phys.* **87**(9), 4548–4552 (2000).
13. S. Palmier, S. Garcia, L. Lemaître, M. Loiseau, T. Donval, J. L. Rullier, I. Tovena, and L. Servant, "Surface particulate contamination of the LIL optical components and their evolution under laser irradiation," in *Laser-Induced Damage in Optical Materials: 2006*, vol. 6403 G. J. Exarhos, A. H. Guenther, K. L. Lewis, D. Ristau, M. J. Soileau, and C. J. Stolz, eds., International Society for Optics and Photonics (SPIE, 2007), pp. 301–310.
14. P. A. Baisden, L. J. Atherton, R. A. Hawley, T. A. Land, J. A. Menapace, P. E. Miller, M. J. Runkel, M. L. Spaeth, C. J. Stolz, T. I. Suratwala, P. J. Wegner, and L. L. Wong, "Large optics for the national ignition facility," *Fusion Sci. Technol.* **69**(1), 295–351 (2016).
15. M. L. Spaeth, P. J. Wegner, T. I. Suratwala, M. C. Nostrand, J. D. Bude, A. D. Conder, J. A. Folta, J. E. Heebner, L. M. Kegelmeyer, B. J. MacGowan, D. C. Mason, M. J. Matthews, and P. K. Whitman, "Optics recycle loop strategy for NIF operations above UV laser-induced damage threshold," *Fusion Sci. Technol.* **69**(1), 265–294 (2016).
16. F. Tournemene, S. Bouillet, C. Rouyer, B. D. C. Fernandes, G. Gaborit, C. Leymarie, and B. Battelier, "Visual defects diffraction in high power lasers: impact on downstream optics," in *Laser-Induced Damage in Optical Materials 2017*, vol. 10447 (SPIE, 2017), pp. 166–175.
17. L. Mascio-Kegelmeyer, "Machine learning for managing damage on NIF optics," in *Laser-induced Damage in Optical Materials 2020*, V. E. Gruzdev, C. W. Carr, D. Ristau, and C. S. Menoni, eds. (SPIE, 2020).
18. C. Lacombe, G. Hallo, M. Sozet, P. Fourtillan, R. Diaz, S. Vermersch, and J. Neauport, "Dealing with LMJ final optics damage: post-processing and models," in *Laser-induced Damage in Optical Materials 2020*, V. E. Gruzdev, C. W. Carr, D. Ristau, and C. S. Menoni, eds. (SPIE, 2020).
19. J. Folta, M. Nostrand, J. Honig, N. Wong, F. Ravizza, P. Geraghty, M. Taranowski, G. Johnson, G. Larkin, D. Ravizza, J. Peterson, B. Welday, and P. Wegner, "Mitigation of laser damage on national ignition facility optics in volume production," in *SPIE Proceedings*, G. J. Exarhos, V. E. Gruzdev, J. A. Menapace, D. Ristau, and M. Soileau, eds. (SPIE, 2013).

20. P. Cormont, A. Bourgeade, S. Cavaro, T. Donval, T. Doualle, G. Gaborit, L. Gallais, L. Lemaignère, and J.-L. Rullier, "Relevance of carbon dioxide laser to remove scratches on large fused silica polished optics," *Adv. Eng. Mater.* **17**(3), 253–259 (2015).
21. T. Doualle, L. Gallais, S. Monneret, S. Bouillet, A. Bourgeade, C. Ameil, L. Lemaignère, and P. Cormont, "Development of a laser damage growth mitigation process, based on co2 laser micro processing, for the laser megajoule fused silica optics," in *SPIE Proceedings*, G. J. Exarhos, V. E. Gruzdev, J. A. Menapace, D. D. Ristau, and M. M. Soileau, eds. (SPIE, 2016).
22. A. Conder, J. Chang, L. Kegelmeyer, M. Spaeth, and P. Whitman, "Final optics damage inspection (FODI) for the national ignition facility," in *SPIE Proceedings*, A. A. S. Awwal, K. M. Iftakharuddin, and S. C. Burkhart, eds. (SPIE, 2010).
23. F. Wei, F. Chen, B. Liu, Z. Peng, J. Tang, Q. Zhu, D. Hu, Y. Xiang, N. Liu, Z. Sun, and G. Liu, "Automatic classification of true and false laser-induced damage in large aperture optics," *Opt. Eng.* **57**(5), 1 (2018).
24. G. Hallo, C. Lacombe, M. Fouchier, M. Zerrad, J. Néauport, and F. Hild, "Optical model-based calibration of gray levels for laser damage size assessment," Submitted to *Optics Letters* –, – (2022).
25. J. D. Nicola, T. Bond, and M. Bowers, *et al.*, "The national ignition facility: laser performance status and performance quad results at elevated energy," *Nucl. Fusion* **59**(3), 032004 (2019).
26. R. A. Negres, D. A. Cross, Z. M. Liao, M. J. Matthews, and C. W. Carr, "Growth model for laser-induced damage on the exit surface of fused silica under UV, ns laser irradiation," *Opt. Express* **22**(4), 3824 (2014).
27. M. Veinhard, O. Bonville, S. Bouillet, R. Courchinoux, R. Parreault, J.-Y. Natoli, and L. Lemaignère, "Parametric study of laser-induced damage growth in fused silica optics with large beams at 351 nm part 1: stochastic approach," *Appl. Opt.* **59**(31), 9643 (2020).
28. R. A. Negres, G. M. Abdulla, D. A. Cross, Z. M. Liao, and C. W. Carr, "Probability of growth of small damage sites on the exit surface of fused silica optics," *Opt. Express* **20**(12), 13030 (2012).
29. R. A. Negres, M. A. Norton, Z. M. Liao, D. A. Cross, J. D. Bude, and C. W. Carr, "The effect of pulse duration on the growth rate of laser-induced damage sites at 351 nm on fused silica surfaces," in *SPIE Proceedings*, G. J. Exarhos, V. E. Gruzdev, D. Ristau, M. J. Soileau, and C. J. Stolz, eds. (SPIE, 2009).
30. L. Lemaignère, K. Gaudfrin, T. Donval, J. Natoli, J.-M. Sajer, D. Penninckx, R. Courchinoux, and R. Diaz, "Laser-induced damage of fused silica optics at 355 nm due to backward stimulated brillouin scattering: experimental and theoretical results," *Opt. Express* **26**(9), 11744 (2018).
31. X. Chai, P. Li, J. Zhao, G. Wang, D. Zhu, Y. Jiang, B. Chen, Q. Zhu, B. Feng, L. Wang, and Y. Jing, "Laser-induced damage growth of large-aperture fused silica optics under high-fluence 351 nm laser irradiation," *Optik* **226**, 165549 (2021).
32. Z. M. Liao, B. Raymond, J. Gaylord, R. Fallejo, J. Bude, and P. Wegner, "Damage modeling and statistical analysis of optics damage performance in MJ-class laser systems," *Opt. Express* **22**(23), 28845 (2014).
33. J. Neauport, L. Lemaignère, H. Bercegol, F. Pilon, and J.-C. Birolleau, "Polishing-induced contamination of fused silica optics and laser induced damage density at 351 nm," *Opt. Express* **13**(25), 10163–10171 (2005).
34. R. Catrin, J. Neauport, D. Taroux, P. Cormont, C. Maunier, and S. Lambert, "Magnetorheological finishing for removing surface and subsurface defects of fused silica optics," *Opt. Eng.* **53**(9), 092010 (2014).
35. M. Veinhard, O. Bonville, S. Bouillet, R. Courchinoux, R. Parreault, J.-Y. Natoli, and L. Lemaignère, "Parametric study of laser-induced damage growth in fused silica optics with large beams at 351 nm part 2: fractal analysis," *Appl. Opt.* **59**(31), 9652 (2020).
36. R. Diaz, R. Courchinoux, J. Luce, C. Rouyer, J.-L. Rullier, J.-Y. Natoli, and L. Lemaignère, "Experimental evidence of temporal and spatial incoherencies of q-switched nd:YAG nanosecond laser pulses," *Appl. Phys. B* **121**(4), 439–451 (2015).
37. D. Penninckx, J. Luce, R. Diaz, O. Bonville, R. Courchinoux, and L. Lemaignère, "Multiple-frequency injection-seeded nanosecond pulsed laser without parasitic intensity modulation," *Opt. Lett.* **41**(14), 3237 (2016).
38. P. Grua, L. Lemaignère, M. Chambonneau, R. Courchinoux, and J. Néauport, "Nanosecond laser damage initiation at 035 μm in fused silica," *Opt. Lett.* **43**(11), 2692 (2018).
39. S. Bouillet, C. Ameil, V. Beau, O. Bonville, S. Cavaro, R. Courchinoux, J. Daurios, T. Donval, L. Eupherte, S. Fréville, G. Gaborit, I. Lebeaux, C. Leymarie, S. Martin, R. Parreault, G. Razé, N. Roquin, and L. Lemaignère, "Large optics metrology for high-power lasers," *J. Opt. Soc. Am. A* **36**(11), C95–C103 (2019).
40. O. Morice, "Miró: Complete modeling and software for pulse amplification and propagation in high-power laser systems," *Opt. Eng.* **42**(6), 1530 (2003).
41. G. Hallo, C. Lacombe, J. Néauport, and F. Hild, "Detection and tracking of laser damage sites on fused silica components by digital image correlation," *Opt. Lasers Eng.* **146**, 106674 (2021).
42. L. M. Kegelmeyer, P. W. Fong, S. M. Glenn, and J. A. Liebman, "Local area signal-to-noise ratio (LASNR) algorithm for image segmentation," in *Applications of Digital Image Processing XXX*, A. G. Tescher, ed. (SPIE, 2007).
43. A. K. Burnham, M. J. Runkel, S. G. Demos, M. R. Kozlowski, and P. J. Wegner, "Effect of vacuum on the occurrence of UV-induced surface photoluminescence, transmission loss, and catastrophic surface damage," in *SPIE Proceedings*, E. W. Taylor, ed. (SPIE, 2000).